Drug Metabolism Reviews

http://informahealthcare.com/dmr
ISSN: 0360-2532 (print), 1097-9883 (electronic)

Drug Metabolism Reviews, Early Online: 1–10
 DOI: 10.3109/03602532.2015.1058818

informa
healthcare

REVIEW ARTICLE

Photothermal confocal multicolor microscopy of nanoparticles and nanodrugs in live cells

Dmitry A. Nedosekin[1], Stephen Foster[1], Zeid A. Nima[2], Alexandru S. Biris[2], Ekaterina I. Galanzha[1], and Vladimir P. Zharov[1]

[1]Arkansas Nanomedicine Center, University of Arkansas for Medical Sciences, Little Rock, AR, USA and [2]Center for Integrative Nanotechnology Sciences, University of Arkansas at Little Rock, Little Rock, AR, USA

Abstract

Growing biomedical applications of non-fluorescent nanoparticles (NPs) for molecular imaging, disease diagnosis, drug delivery, and theranostics require new tools for real-time detection of nanomaterials, drug nano-carriers, and NP-drug conjugates (nanodrugs) in complex biological environments without additional labeling. Photothermal (PT) microscopy (PTM) has enormous potential for absorption-based identification and quantification of non-fluorescent molecules and NPs at a single molecule and 1.4 nm gold NP level. Recently, we have developed confocal PTM providing three-dimensional (3D) mapping and spectral identification of multiple chromophores and fluorophores in live cells. Here, we summarize recent advances in the application of confocal multicolor PTM for 3D visualization of single and clustered NPs, alone and in individual cells. In particular, we demonstrate identification of functionalized magnetic and gold–silver NPs, as well as graphene and carbon nanotubes in cancer cells and among blood cells. The potential to use PTM for super-resolution imaging (down to 50 nm), real-time NP tracking, guidance of PT nanotherapy, and multiplex cancer markers targeting, as well as analysis of non-linear PT phenomena and amplification of nanodrug efficacy through NP clustering and nano-bubble formation are also discussed.

Keywords

Blood cells, cancer cells, gold nanorods, graphene, magnetic beads, nanoparticles, photothermal microscopy, toxicity

History

Received 9 March 2015
Revised 22 April 2015
Accepted 19 May 2015
Published online 1 July 2015

Introduction

The rapidly growing range of applications for the advanced nanoparticles (NPs) used as biosensors, drug carriers, and contrast agents for imaging and therapy require techniques for detection of NPs in complex biological environments with high resolution at single cell and NP levels. For example, gold and magnetic NPs, advanced golden carbon nanotubes, photo-switchable NPs, and various nanoparticle-drug conjugates proposed as novel imaging and therapeutic agents have been successfully used for the detection and identification of tumor cells, mapping sentinel lymph nodes, or cancer theranostics (integrated diagnosis and therapy) (Coll, 2010). Imaging of NPs inside the cells is important to optimize NP delivery with a focus on control of NP clustering during internalization to enhance imaging contrast and therapy efficiency. Indeed, such clustering, on the one hand, can dramatically amplify signals of different origins from clustered NPs (Nima et al., 2014); on the other hand, it can enhance efficiency of localized photothermal (PT) therapy (Shao et al., 2013). Cellular NP biodistribution is important to determine a link between local NP concentration and cytotoxicity (Alkilany & Murphy, 2010). In PT therapy without dynamic control of NP concentration, the temperature-induced protein denaturation or mechanical disruption of cellular structures by laser-generated nano-bubbles around overheated NPs (Zharov, 2011) may be insufficient to produce the desired local therapeutic effects, or, conversely, strong PT phenomena can destroy surrounding healthy tissues (Shao et al., 2013; Zharov et al., 2003).

Among diverse imaging methods (e.g. multiphoton microscope, Raman, or transient absorption), confocal fluorescence microscopy remains the most widely used powerful biological tool, capable of 3D imaging of fluorescent NPs, in particular quantum dots (Coll, 2010). However, in order to visualize non-fluorescent NPs using fluorescence-based methods, such NPs should be labeled using fluorescent tags. Growing evidence demonstrates possible toxicity and labeling-induced change in NPs and cellular properties (Coll, 2010; Mérian et al., 2012). Transmission and dark-field microscopy methods face challenges due to low sensitivity of absorption measurements and the presence of light scattering artifacts among cells. Indeed, absorption and scattering cross section of gold NPs varies as the third and sixth power of the NP size, respectively (Van Dijk et al., 2006). Hence, scattering contrast for small particles is low, while cell structures

Address for correspondence: Dmitry A. Nedosekin and Vladimir P. Zharov, Arkansas Nanomedicine Center, University of Arkansas for Medical Sciences, 4301 W. Markham St. Little Rock, AR 72205, USA. E-mail: DNedosekin@uams.edu. (D.A.Nedosekin), E-mail: zharovvladimirp@uams.edu (V.P.Zharov)

provide a significant heterogeneous background. Nonetheless, dark-field microscopy has found wide use in the detection, identification, and tracking of various NPs with the assistance of multispectral imaging for spectral identification of NPs among other scatters (Jayanna et al., 2010; Lee & Tung, 2012; Mustafa et al., 2013). Still, limited axial resolution of dark-field imaging and low scattering contrast for small-sized NPs hinder certain applications of this technique (Sathuluri et al., 2011; Weinkauf & Brehm-Stecher, 2009).

Among the tools developed for visualization of nanomaterials in biological samples, one group of methods stands out as sensitive toward non-fluorescent NPs while non-sensitive toward light scattering in the sample. Most of the light energy absorbed by non-fluorescent NPs is transformed through non-radiative relaxation into heat, which can be quantified through PT phenomena, phase-contrast, thermal lens, or heterodyne detection methods (Brusnichkin et al., 2010; Cognet et al., 2008; Gaiduk et al., 2010; Moreau & Loriette, 2006; Nedosekin et al., 2014; Selmke et al., 2012b). In these methods, the temperature-dependent refractive index changes are measured using a second probe laser beam as it undergoes phase change, defocuses, or is being scattered, respectively. These techniques, including PT microscopy (PTM), have enormous potential in the biomedical imaging of neurons (Thoumine et al., 2008), blood cell markers (Kimura et al., 2001), gene expression analysis (Blab et al., 2006), mitochondria imaging (Brusnichkin et al., 2010; Nedosekin et al., 2012), and optimization of PT therapy (Zharov et al., 2005). The specificity of PTM is similar to that of conventional spectroscopy and derives from intrinsic absorption contrast of endogenous chromophores (Nedosekin et al., 2012) or from the use of low-toxicity small NPs (2–20 nm) (Blab et al., 2006; Cognet et al., 2003; Lasne et al., 2006) conjugated to molecular specific antibodies. PTM offers the highest absorption sensitivity providing the unprecedented capability for label-free detection of single molecules (Gaiduk et al., 2010) (i.e. sensitivity comparable to that of fluorescence methods). Using signal generation approaches similar to PTM, photoacoustic microscopy (PAM) provides data on sample absorption (absorption → heating) (Ntziachristos, 2010; Wang & Hu, 2012). However, PTM provides a much higher sensitivity (≥30- to 50-fold) *in vitro* (Gaiduk et al., 2010; Nedosekin et al., 2010, 2012) and does not require an acoustic contact between the sample and transducer (Ntziachristos, 2010; Wang & Hu, 2012).

Nonetheless, most previous PTM modalities lacked a crucial ability: imaging has been performed preferentially in 2D scale (Cognet et al., 2008). Moreover, in most of the applications, cells adhering to the substrate surface were used that improved the scattering background (Bogart et al., 2012), but limited PTM utility for 3D absorption reconstruction. The imaging of cells and NPs in suspension may provide multiple benefits including study of non-cultivated cells extracted after tumor biopsy or from various biological liquids including blood, lymph, and cerebrospinal fluid (Nedosekin et al., 2013a, b).

Recently, we have developed confocal spectral PTM and demonstrated its application for 3D spectral imaging and identification of multiple chromophores and fluorophores in single live cells. However, its capability for 3D imaging of NPs alone or in cells has not been discussed in detail yet. Here, we fill this gap by summarizing our recent results on application of an advanced confocal PTM platform for visualization and identification of functionalized magnetic NPs among intrinsic cellular structures, study the interaction of graphene with blood and cancer cells, and produce images of Au–Ag hybrid NPs in various environments.

Principles of PT-based methods

In time-resolved, dual-beam (pump-probe), confocal PTM featuring a thermal lens schematic (Figure 1A and B), excitation laser pulses (also termed pump pulses) induce temperature-dependent variations of the refractive index around endogenous absorbing cellular structures or NPs. This defocuses/diffracts a second collinear continuous wave (CW) laser probe beam (thermal lens effect). Specifically, the temperature distribution is transformed into a refraction distribution, n_T $(dn/dT)T_{max.}$ Diffraction of the probe beam is detected as a modulation of the beam's intensity in the far-field

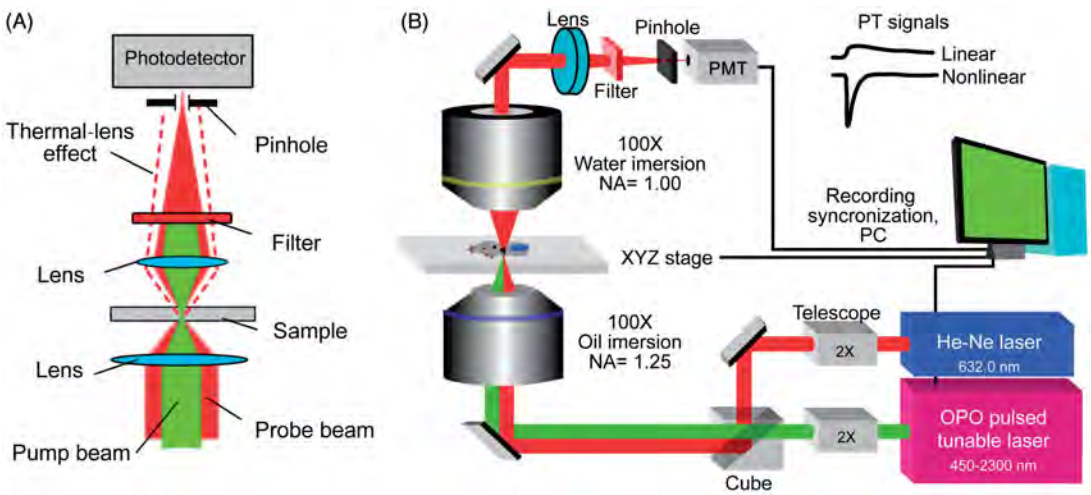

Figure 1. Confocal high-resolution PTM: (A) principles of confocal PT detection and (B) schematics of spectral PTM. Illustrations were adopted from Nedosekin et al. (2014).

using photodiode and a pinhole. Absorption of short laser pulses results in linear PT signals having an initial peak associated with rapid heating of cellular chromophores or NPs, as well as slower (ns to μs) heat transfer into the surrounding medium (Zharov, 2011; Zharov et al., 2005). For spherical targets 5 nm to 5 μm in size, thermal relaxation times are in the range of 40 ps to 40 μs. In the non-linear mode, absorption of a laser pulse overheats the surrounding medium inducing the formation of gas nano-bubbles. This results in the appearance of a sharp negative peak in the PT signal associated with refraction and scattering of the probe beam by the nano- and micro-bubbles.

Clustering of NPs may dramatically enhance non-linear PT contrast and increase therapeutic efficiency of the nanodrugs. According to our nanocluster PTM model (Zharov et al., 2005), a short laser pulse initially interacts with individual absorbing biomolecules or NPs. Most of these absorbers, typically nanoscale in size, form nanoclusters in various biological environments, such as cytochromes in mitochondria, melanin in melanosomes, and NPs around clustered biomarkers. Due to the proximity of these nano-absorbers in clusters, laser-induced optical, thermal, acoustic, and other PT-based phenomena may overlap spatially and temporally, causing linear and especially non-linear, synergistic enhancement (10- to 100-fold) of PT effects (Zharov, 2011; Zharov & Lapotko, 2005). These effects become extremely sensitive to the spatial organization of nanoabsorbers in the nanoclusters and to their spatial relocation during cell metabolism, apoptosis, and necrosis [e.g. shrinking, swelling, or Cyt c relocation (Zharov et al., 2006a)] or due to natural aggregation of endogenous particles.

Confocal PTM schematics

The confocal PT microscope previously described elsewhere (Brusnichkin et al., 2010; Nedosekin et al., 2012, 2014) was built on the technical platform of an Olympus IX81 inverted microscope (Olympus America, Inc., Center Valley, PA) using a tunable, optical, parametric oscillator (OPO; Opolette HR 355 LD, Opotek, Inc., Carlsbad, CA) with 5-ns pulse duration, 100 Hz pulse repetition rate, and 410–2500 nm spectral tuning range. PT effects were probed using a He–Ne probe beam collinear with the pump laser (model 117A, Spectra-Physics, Inc., Mountain View, CA; wavelength, 633 nm; 1.4 mW). Laser beams were focused on the sample using 100 × oil-immersion objective (DPlan 100, NA 1.25, Olympus, Inc.), 40 × (Ach, NA 0.65, Olympus, Inc.) and a custom objective built using a single achromatic doublet lens (AC127-025-A-ML, Thorlabs, Inc., Newton, NJ) for high- and low-resolution PT imaging, respectively. Sample images were acquired by raster scanning the sample using a two-dimensional (X–Y) stage (H117 ProScan II, Prior Scientific, Inc., Rockland, MA), scanning step 0.25–1 μm. Focusing along the *Z*-axis was performed by moving the microscope objective axially (a minimum of 50-nm step). Probe laser light transmitted through the sample was collected using either 100 × water-immersion (LUMPlanFl 100, NA 1.00, Olympus, Inc.) or 40 × objective (Ph3 DL, NA 0.55, Nikon Inc., Los Angeles, CA). Total probe beam power was only 140 μW in the sample plane. PT signals were detected using amplified photodiode (PDA36A, Thorlabs, Inc). To provide confocal PT detection, a 50-nm pinhole before the photodiode was carefully adjusted to be on a plane one Rayleigh range away from the probe beam waist image plane. The pump laser waist in the sample was carefully adjusted to match the probe beam location. PT signals were recorded using a 200-MHz analog-to-digital converter board (National Instruments Corp., Austin, TX, PCI-5152, 12-bit card, 128 MB of memory) and analyzed by custom software (LabVIEW 8.5 complex; National Instruments). A Dell Precision 690 work-station provided signal acquisition/processing, synchronization of the excitation laser, and translation-stage control. The imaging speed of the current prototype was primarily limited by the pulse repetition rate of the laser source (100 Hz); therefore, a typical PT image (50 × 50 pixels) was acquired in < 40 s (no averaging) or in 4–5 min (averaging of 10 PT signals). In enhanced dark-field microscopy (EDFM) mode, an enhanced illuminator (CytoViva Inc., Auburn, AL) replaced the custom light collection condenser used for PT imaging. The illuminator consisted of a CytoViva 150 condenser and fiber optic light guide connected to a Solarc 24W metal halide light source (Welch Allyn, Skaneateles Falls, NY). A 100 × oil objective with an iris (Olympus UPlanAPO fluorite, N.A. 1.35–0.55) and a color camera (DP72, Olympus America Inc.) were used to acquire sample images. The EDFM illuminator dramatically increased the scattering contrast of NPs inside cells.

Resolution of confocal PTM

Accurate assessment of confocal PTM resolution is a crucial task; however, it is hindered by the lack of a well-established methodology for PT techniques. To correctly estimate PTM resolution, we used (1) magnification reference standard (MRS-4, TedPella, Inc., Redding, CA) featuring Cr/CrO_2 patterns on transparent quartz substrate; (2) 75-nm gold nanowires; and (3) gold NPs of varying diameter. Lateral PTM resolution was determined by a line-scan method with 10-nm step size, and axial resolution was assessed by transverse translation of the focusing objective.

PTM imaging resolution is limited by the diffraction of the light as in most optical microscopy. It was experimentally verified using a Cr/CrO_2 pattern having well-defined edges (Figure 2A). Axial and lateral resolution in low NA mode (10 × objective, NA 0.3) was estimated to be 0.99 ± 0.1 μm and 7.5 ± 0.3 μm, respectively. For high-NA 100 × objectives (NA of 1.25), the lateral and axial resolution of the confocal PTM (in linear mode) was experimentally estimated at 260 ± 20 and 900 ± 100 nm, respectively, by imaging single 75-nm gold nanowires (Figure 2B and C). PTM with low NA quickly estimates cell location, while high NA can provide fine localization of NPs in living cells.

3D visualization of cancer cell markers' distribution using intrinsic and NP-based PT molecular contrast agents

The functionalization of NPs with antibodies or other ligands specific for selected cancer markers, as well as efficient control of molecular targeting of these markers by conjugated NPs, is crucial to optimize nanodiagnostics and

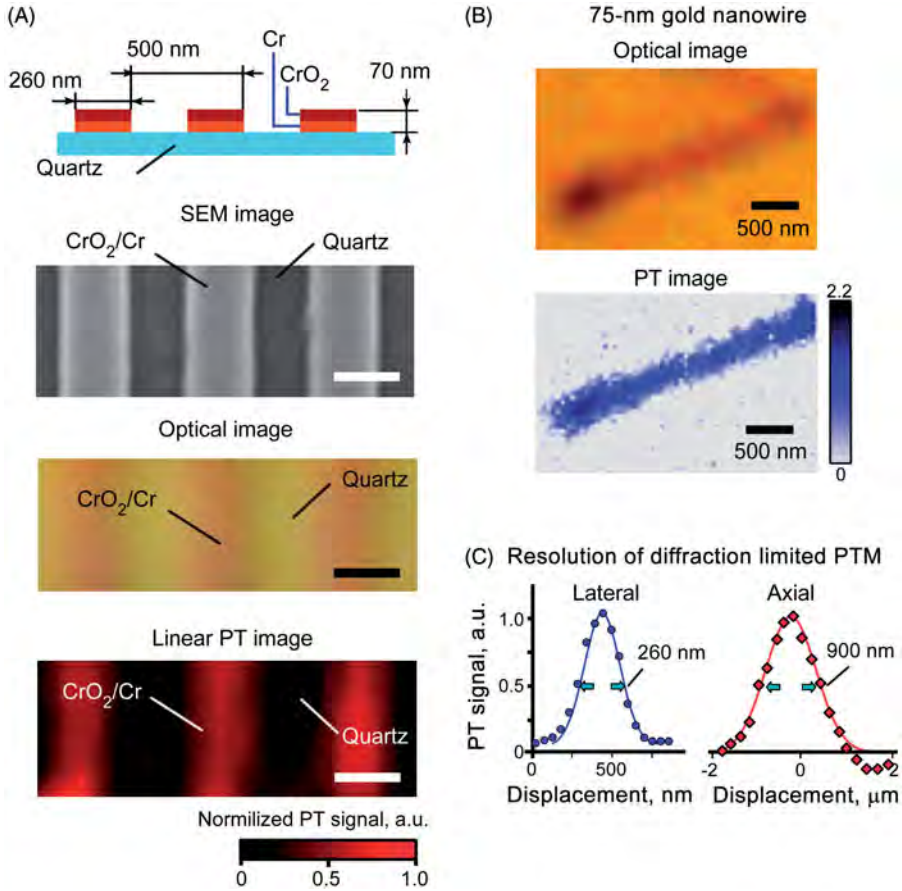

Figure 2. Calibration of PTM resolution using reference standards. (A) MRS-4 reference standard (from top to bottom): schematic of sample, scanning electron microscopy (SEM), optical and linear PT imaging, respectively. Scale bar is 250 nm. (B) Optical and PT imaging of a single 75-nm gold nanowire. (C) Lateral and axial resolution of confocal PTM. Laser pump parameters: wavelength, 532 nm; energy fluence, 100 mJ/cm^2; beam diameter, 250 nm. Panels A and C were adopted from Nedosekin et al. (2014).

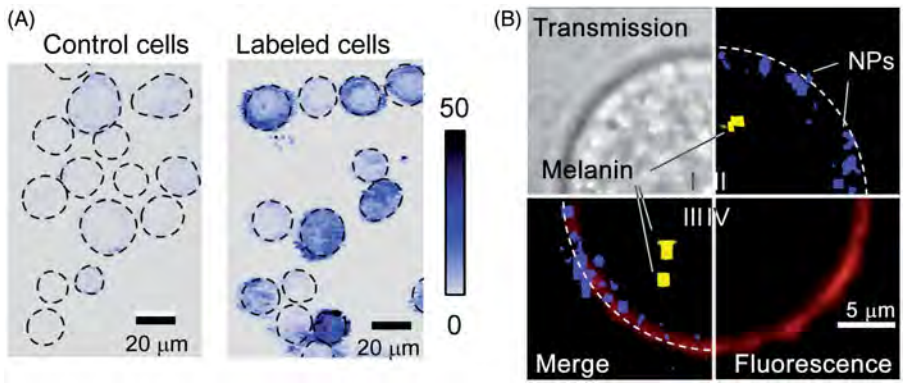

Figure 3. PT imaging of intrinsic cellular and exogenous PT contrast agents in SK-mel-1 melanoma cancer cells. (A) Low resolution 2D PT imaging of cells before and after molecular targeting of MCSP surface receptors by anti-MCSP 50-nm magnetic NPs: dash lines show cell boundaries. (B) High resolution 2D transmission (I), confocal PT at 532 nm (II), fluorescence (IV), and combined (III) images of melanoma cell targeted by anti-MCSP magnetic NPs and anti-MCSP–PE fluorescent antibody (orange dye). Panel B was adopted from Galanzha & Zharov (2013).

nanotherapeutics. In studies related to early detection of melanoma metastases (Nedosekin et al., 2010, 2012, 2013b), a confocal PTM integrated with fluorescence microscopy was deployed to verify molecular targeting of melanoma-associated chondroitin sulfate proteoglycan (MCSP) receptors of human melanoma cells (SK-mel-1 cell line). These SK-mel-1 cells were cultured according to standard procedures (Nedosekin et al., 2012) and labeled with 50-nm anti-MCSP magnetic NPs according to the NP manufacturer's protocols using triple centrifugation at 300 × *g* (10 min) to remove unbound NPs. After incubation, low resolution rapid PT imaging (Figure 3A) confirmed that the absorption of ~50% cells significantly (5- to 10-fold) increased due to the presence of light-absorbing NPs. This finding is in line with our previous data (Galanzha & Zharov, 2013). To prove that NPs indeed targeted the MCSP cell surface marker, concurrent cell targeting was performed using a cocktail of conventional phycoerythrin (PE) dye conjugated with anti-MCSP Ab with anti-MCSP magnetic NPs. Integrated fluorescence and PT imaging of cells in suspension revealed spatial coincidence of fluorescence and PT signals, indicating that NPs specifically labeled the MCSP surface marker (Figure 3B, panel III). For both unlabeled and labeled cells, the confocal PTM platform can create 3D mapping of marker spatial distribution by obtaining sequent multiple 2D PT images acquired along the laser axis (Figure 4A). As expected, for unlabelled SK-mel-1 melanoma cells, PT imaging revealed highly localized structures associated with individual and clustered nano-sized particles of melanin located preferentially in the cell cytoplasm. Cells targeted by

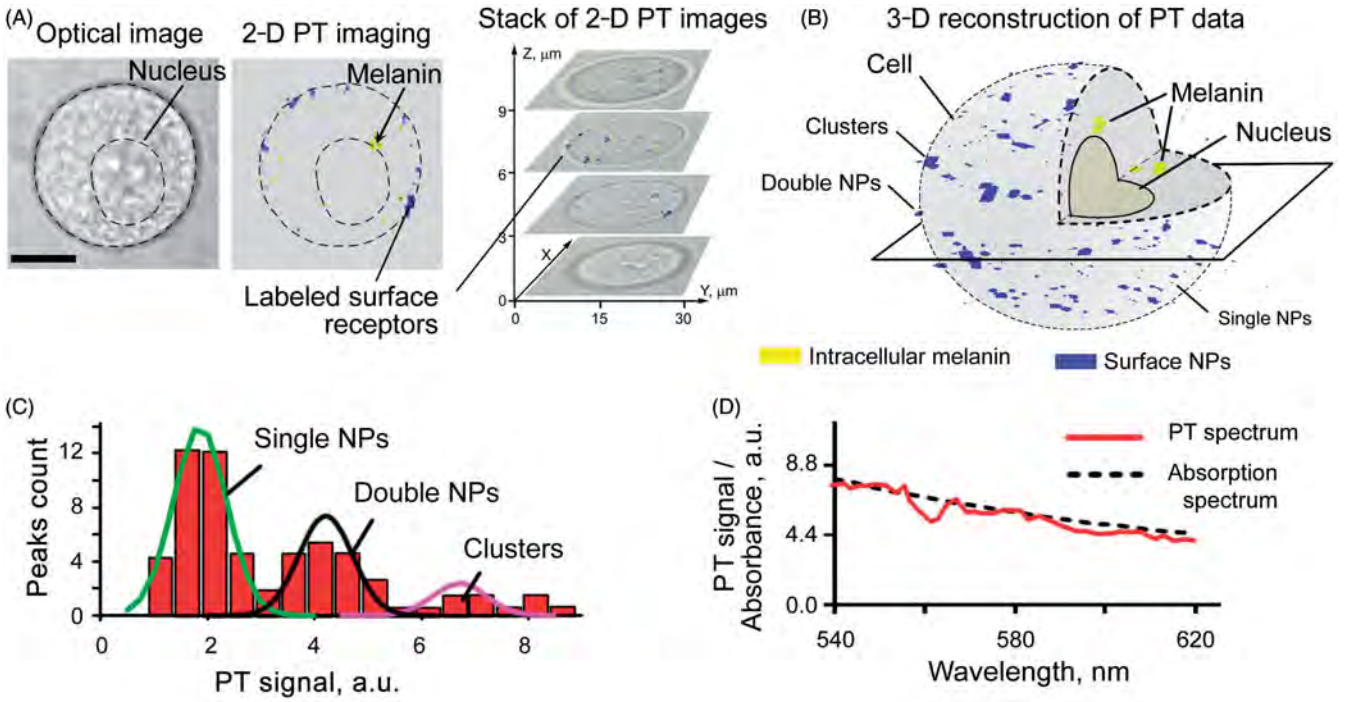

Figure 4. PTM analysis of the volume distribution of cellular intrinsic and exogenous markers. (A) Sequent 2D PT images of different cross sections of a cell targeted by anti-MCSP 50-nm magnetic NPs and a corresponding stack of 2D PT images. (B) 3D spatial reconstruction of surface MCSP receptors (blue) and intracellular melanin (yellow) distribution. (C) Histogram of PT signal amplitudes for magnetic NPs on the cell surface. (D) PT spectrum of magnetic NPs on cell membrane (solid) and conventional absorption spectrum of the same NPs in solution (dash). Laser parameters: wavelength, 600 nm; energy fluence, 0.2 J/cm^2. Panels B, and C were adopted from Galanzha & Zharov (2013).

magnetic NPs demonstrated spatial PT signatures (Figure 4A, right) associated with both intrinsic melanin NPs inside the cell and with magnetic NPs on the cell membrane. Analysis of a stack of 2D PT images confirmed surface distribution of MCSP markers and of intracellular accumulation of melanin (Figure 4B) and allowed us to reconstruct a 3D distribution (Figure 4B) of cell absorption profiles (Supplemental Videos S1 and S2). Thus, for melanoma cells labeled with NP–MCSP conjugates, PT signals exceeding background levels were acquired in >70% of the cells, implying an advantage to combining molecular labeling with intrinsic markers. These results are in agreement with conventional flow cytometry (FACS Caliber system with Cell Quest Pro software, San Jose, CA) that indicated MCSP expression in 51% of cells (against 52% obtained with PTM). Notably, a reverse relation between melanin content quantified by PTM and MCSP expression (Galanzha & Zharov, 2012; Nedosekin et al., 2012) resulted in high PT contrast for almost all of the cells – either through NP labeling or due to natural melanin pigmentation.

Using an analysis of NP-associated PT signal amplitudes, we distinguished single NPs from clustered NPs around single and clustered markers, which revealed a certain level of marker spatial heterogeneity (Figure 4C). Gaussian curves illustrated a hypothesis that single, double, and clustered NPs occupied the detection volume. NP clusters provided higher PT signals compared to single NPs (10- to 20-fold in non-linear mode) (Nedosekin et al., 2014). PT spectroscopy of labeled cells and control NPs in solution allowed us to acquire spectral signatures from cell-surface bound NPs (Figure 4D). However, as the absorption spectra of melanin and magnetic NPs are similar, only the data on spatial location of the absorbing zones permitted reliable identification (Figure 3D).

PTM-surface enhanced Raman scattering (SERS) identification of cancer cells labeled by functionalized, multimodal, silver-coated, gold nanorods

Nanotechnology-based, molecular-specific contrast agents have been extensively explored for identification of cancer cells among normal ones for early cancer diagnosis. However, the specificity of simultaneous identification of multiple biomarkers is often limited by spectral overlapping of NP signatures. Recently, we enhanced both molecular and spectral specificity of detection using tunable silver-gold nanorods (SGNRs) (Figure 5A) as multimodal SERS – PT contrast agents. Bi-metallic nanorods were based on a core–shell technology and featured a 1.7 nm thick silver shell covering the gold core. The gold nanorod (GNR) core's length and diameter were approximately 36 and 12 nm, respectively, with a spectral absorption maximum at 766 nm (Figure 5B) before and at 740 nm after applying the silver coating. SGNRs demonstrated a significant increase in SERS contrast compared to bare GNRs and were conjugated with a unique combination of a Raman-active molecule and breast cancer specific antibodies (EpCAM, CD44, Keratin 18 or anti-IGF-I). Accumulation of SGNRs on the surface of targeted breast cancer cells (MCF7) after 30 min of incubation was independently confirmed by dark-field (scattering) technique and PTM along with more classic scanning electron microscopy and elemental analysis mapping (Figure 5). However, the significant light scattering of all of the cells and of white

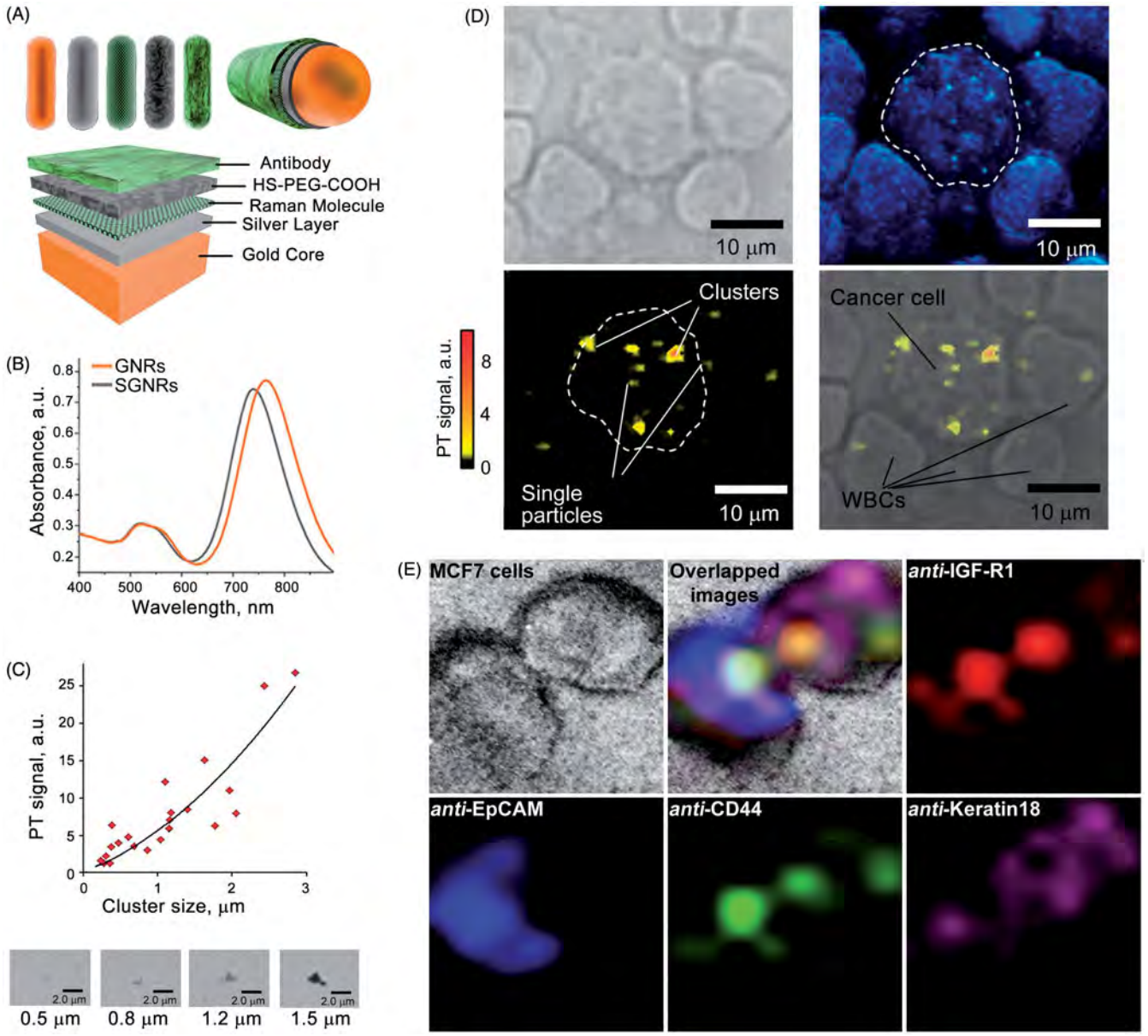

Figure 5. Visualization of NPs inside the cells. (A) Schematic diagram of gold nanorods (GNRs) coated with silver (SGNRs); (B) Optical absorption spectra of GNRs and SGNRs; (C) PT signals from clustered SGNRs. (D) Image of a single cancer cell targeted by SGRNs. From left to right: transmission, enhanced dark-field, PTM, and merged images, respectively. (E) 2D SERS mapping of MCF7 breast cancer cells labeled with a cocktail of 4 SGNRs conjugated to anti-IGF-R1, anti-EpCAM, anti-CD44, and anti-Keratin18 antibodies. Illustrations were adopted from Nima et al. (2014).

blood cells (WBCs), in particular, reduced the sensitivity of the dark-field imaging, thus hindering identification of the SGNRs in the scattering cellular background. This technique is currently limited by 2D scale and thus was not able to identify whether NPs were on the cell surface or inside the cell. The confocal PTM tool is free of light-scattering artifacts and can provide 3D NP distribution allowing the identification of NP position either on cell surfaces or inside cells. According to our preliminary data, initially SGNRs are localized on the cell surface around targeted surface markers, forming small clusters around densely localized markers (Nima et al., 2014). Later SGNRs were internalized through the membrane into the cytoplasm and formed larger clusters significantly amplifying both PT (Figure 5C) and SERS signals (Nima et al., 2014). 2D mapping based on the distinct SERS signatures of the SGNRs was used to generate an overlapping four-color cellular map of the individual cancer cells in blood (Figure 5E). Therefore, this approach integrated four layers of identification of an individual CTC, reducing the undesired false-negative, false-positive results.

PT mapping of WBCs spiked with cancer cells revealed that PT signals were preferentially localized in cancer cells only with no significant signals from WBCs. In order to ensure that the SGNRs did not target normal blood cells, we conjugated SGNRs with antibodies specific to WBC receptor CD45. PT mapping confirmed by Raman microscopy indicated that almost no signals originated from the MCF7 cells, with the majority of NPs collocated at the WBCs' surface (Nima et al., 2014). According to the preliminary estimations, the level of non-specific binding of functionalized SGNRs to blood cells was 8%, which is in line with our previous data (Nima et al., 2014). It should be emphasized that NP clustering significantly increased local optical absorption. Possible applications of this effect include

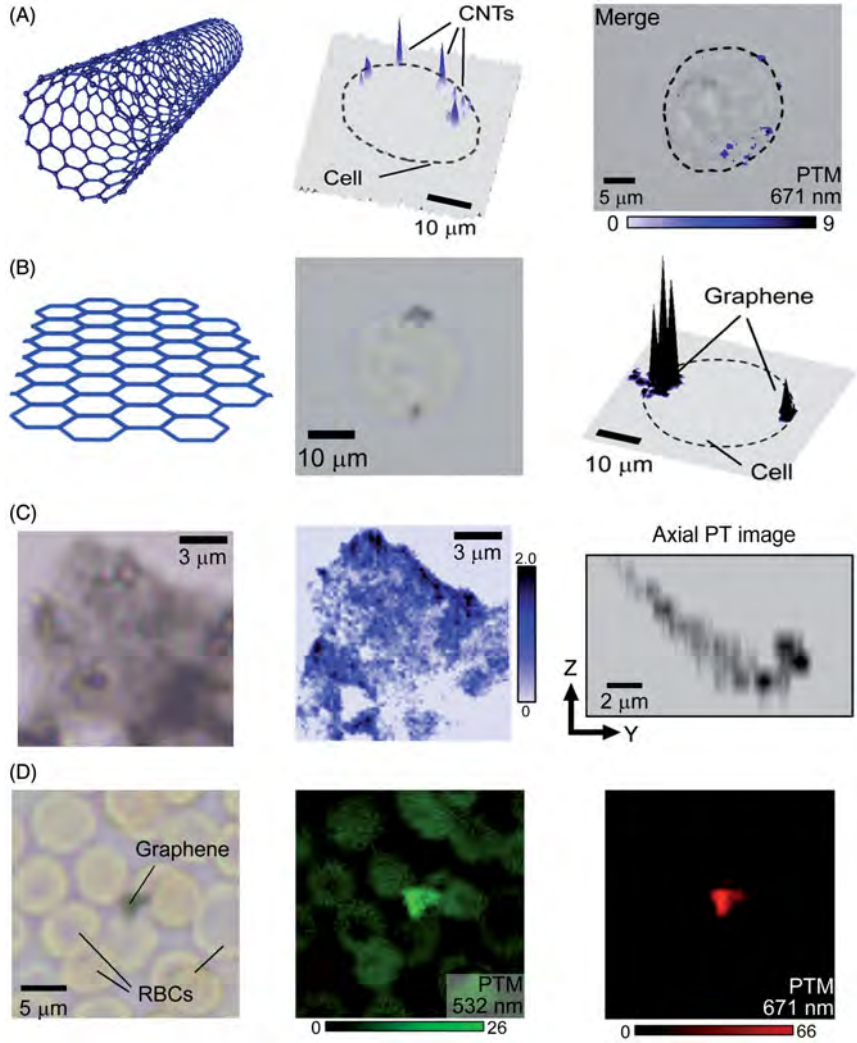

Figure 6. PT imaging of carbon-based nanomaterials. (A), Schematic structure of CNTs (left) and PT images (right) of MDA-MB-231 breast cancer cell with CNTs (incubation parameters: time, 30 min; temperature, 37 °C). (B) Schematic structure of graphene nano-flakes and PT images of MDA-231-MB breast cancer cell with a graphene. (C) Transmission, PT, and axial (ZY plane) PT images of a single graphene flake on a glass substrate. Axial graphene image was reconstructed using 3D spatial distribution and stack of 2D PT images. (D) Multicolor PT imaging of a graphene cluster among RBCs using pump lasers at wavelength of 532 and 671 nm. From left to right: transmission, PT at 532 nm, and PT at 671 nm images, respectively. Laser pump parameter: wavelength, 532 nm in A–D (center), 671 nm in D (right); energy fluence, 0.2 J/cm^2 in A–D (center) and 0.4 J/cm^2 in D (right).

amplification of PT therapeutics through enhanced nano- and micro-bubble formation around over-heated nanoclusters leading to selective, highly localized, mechanical damage of cancer cells (Shao et al., 2013). The simplified formation of therapeutic nano-bubbles around nanoclusters may allow the reduction in laser energy to lower and safer levels or provide the same therapeutic effects in deeper tissues. The advantage of using the SGNRs is represented by their ability not only to target a single breast cancer cell among many million unprocessed blood cells, but also to provide non-overlapping, enhanced, multi-color SERS contrast along with PT and dark-field signatures. This approach could be integrated into a multicolor detection platform with the ability to detect single CTCs in over 10 ml of unprocessed blood in a matter of minutes. The SGNRs also have the capacity for delivering anticancer drug molecules to a single cell or a micro-tumor and releasing them in a controlled manner under laser excitation, further increasing the activity of the drug (Shao et al., 2013).

Imaging of carbon- and graphene-based nanomaterials

Due to the rapidly growing number of biomedical applications of carbon-based nanomaterials (Biris et al., 2013; Nima et al., 2013; Saeed et al., 2014; Zhang et al., 2014), there is an urgent demand for sensitive, rapid, and accurate methods for quantifying nanomaterials, such as carbon nanotubes (CNTs) and graphene-based nanomaterials (GBNs), at the level of a single cell for accurate toxicity evaluation. In particular, weak fluorescence makes it difficult to identify such NPs in biological tissues having strong scattering and autofluorescence backgrounds. In addition, the quantification of carbon-based materials using TEM and similar techniques is challenging in carbon-rich biological samples. In this case, the high absorption contrast of these NPs provides an opportunity for highly sensitive PT-based detection at a single cell level. Indeed, the unique capability of confocal PTM has already been successfully demonstrated for label-free detection of CNTs in thin tissue sections (Nedosekin et al., 2010) and in single cancer cells in the presence of an intrinsic background, in particular cytochromes (Figure 6A). In our preliminary studies, using a combination of confocal PTM and PT spectroscopy, we provided visualization of individual graphene flakes on a glass surface and on a cell membrane (Figure 6B and C). According to absorption data, such flakes were 8 layers thick having an average light transmission of 77%. The 3D reconstruction of flake geometry using confocal PTM schematic (Figure 6C, right and Supplemental Video S3)

has revealed a bell-like shape of the flake even on a flat glass surface. We believe that high resolution data on flake geometry may be essential for understanding how flakes can be internalized by cells and how cell membranes interact with such large sheets of carbon.

PTM has the ability to visualize NPs in the presence of light-absorbing components using multicolor data acquisition. Such methodology was demonstrated by imaging graphene clusters among mouse red blood cells (RBCs). PTM at 532 nm revealed that absorption of the flake is comparable to that of the surrounding single RBCs (Figure 6D, middle), making it difficult to identify this single flake among the cells. However, PT imaging at 671 nm provided higher graphene contrast which significantly reduced the influence of RBC absorption (Figure 6D, right). This example demonstrates the benefits of confocal thermal lens detection schemes of PTM for accurate NP quantification in tissues having significant absorbance (Nedosekin et al., 2012). The benefits of PTM for imaging of NPs absorbing in the near infrared spectral range include reduced influence from the absorption background (e.g. by hemoglobin in RBCs or cytochromes in WBCs) compared to PT imaging of gold NPs at 532 nm (Leduc et al., 2011). The ability of PTM to visualize NPs in the presence of light scattering may facilitate the study of NP-cell interaction in real biological environments. High resolution PTM distinguished NPs on the cell surface from those inside the cell. Confocal PT imaging of gold- and carbon-based NPs' interaction with blood and cancer cells allowed identification of both surface adsorption of graphene (Figures 6B) and non-specific internalization of CNTs (Figure 6A).

Conclusions

Thus, we have developed a technical PTM platform and methodology for confocal PT imaging and spectroscopic identification of various non-fluorescent NPs inside live cells and tissues without the need to use fluorescent labeling and with a minimal sensitivity toward the light scattering background. PTM operating in low-resolution mode provides rapid sample screening, while the high-resolution mode offers the possibility for accurate 3D reconstruction of NP spatial distribution in single cells. Multicolor PTM provides a unique opportunity for spectral identification of the NPs in a complex biological background. Moreover, multiplexing PT measurements with other modalities including SERS microscopy provides unique opportunities for rapid sample screening using pulsed PTM followed by slower Raman spectroscopy of SERS tags in identified regions of interest.

Control over PTM resolution makes it possible to either perform initial screening of the sample to quantify total NP uptake (Cognet et al., 2008; Zharov et al., 2006b) or build a detailed NP distribution map by acquiring multiple high-resolution PT images of a cell at different axial positions (Shao et al., 2013). Sample axial displacement in confocal system produces a PT signal curve with a single maximum compared to a bipolar one in the case of a conventional thermal lens detection scheme (Selmke et al., 2012a,b). This makes it possible to calculate integral sample absorption or even a 3D distribution of the light-absorbing components by combining several 2D PT images acquired along the laser axis. The confocal thermal lens schematics in PTM additionally improve the accuracy of detection in a light-scattering medium (probe intensity is normalized for signal calculations) and can be used with low-intensity probe lasers. We demonstrated PT quantification of various NPs bound to cell membranes, as well as NPs transferred into the cell cytoplasm through non-specific endocytotic uptake.

The novel confocal PTM platform can remedy all previous drawbacks of PTM techniques (Introduction) and thus open a view onto completely unexplored areas of biological research, such as label-free 3D imaging and spectral identification of various NPs in complex biological backgrounds. Due to the time-resolved mode, PTM provides, without the influence of thermal blurring, a high (250–300 nm) diffraction-limited resolution, analogous to other far-field microscopy modalities. Moreover, the integration of the confocal PTM with our earlier concepts of far-field super-resolution PTM beyond the diffraction limit (Nedosekin et al., 2014) and PT lifetime nano-imaging (based on the different cooling times of different-sized targets and on the precise location of the center of the PT diffraction spot) (Nedosekin et al., 2012) will produce a platform for imaging capable at a minimum of estimating the average size of single absorbing targets with dimensions in the range of 5–100 nm and with distances between individual targets as short as 20–50 nm (Nedosekin et al., 2014; Zharov et al., 2003). Strong nano-bubble amplified PT signals in the focal volume can only enhance PTM's capability for super-resolution 3D imaging beyond the diffraction limit down to 50 nm. All of these features open a broad range of applications for confocal PTM: identification of cellular structures in normal and pathologic states, mapping of cancer markers and estimation of their expression, study of cell–NP and laser–NP interactions (e.g. optimization of PT diagnosis and therapy; cancer and infections), testing of new PT nanodrugs (Shao et al., 2013), as well as chemosensitivity, radiation, and toxicity testing for predicting the response of individual tumors and normal cells to therapeutic agents.

Finally, PTM could be complementary to fluorescence microscopy for weakly fluorescent cells. As the basic optical schemes are similar for confocal fluorescence and PT microscopy (e.g. the same pinhole and photodetector can be used in both modes), these two techniques can be integrated to conjointly study cells with different absorption and fluorescence. For example, silver–gold NPs provide reliable molecular targeting of cancer cell markers and can be used together with PTM during an extended period of time. Compared to fluorescent labeling, most NPs have much higher stability enabling samples to be fixed and stored for extremely long periods of time.

Acknowledgements

We would like to acknowledge Nanopartz, Inc. for custom conjugation of gold nanorods and Dr Mazen Juratli for help with the cells' fixation. The editorial assistance of Dr Marinelle Ringer is also acknowledged. We acknowledge the Arkansas Research Alliance Memorandum of Understanding with the Food and Drug Administration (FDA) with the focus on graphene research.

Declaration of interest

The authors declare that there are no conflicts of interest. This work was supported by grants from the National Institute of Health (R01CA131164, R01EB009230, R01EB017217, R21EB0005123, and R21CA139373), the National Science Foundation (DBI-0852737), the award from the Department of Health and Human Services, DoD TATRC program, as well as grants from the Arkansas Bioscience Institute and the Translational Research Institute at the University of Arkansas for Medical Sciences. This work was also supported by the U.S. Food and Drug Administration (award HHSF223201210189C administered through Arkansas Research Alliance). The views presented in this paper are not necessarily those of the US FDA.

References

Alkilany A, Murphy C. (2010). Toxicity and cellular uptake of gold nanoparticles: What we have learned so far? J Nanopart Res 12: 2313–2333.

Biris AR, Pruneanu S, Pogacean F, et al. (2013). Few-layer graphene sheets with embedded gold nanoparticles for electrochemical analysis of adenine. Int J Nanomedicine 8:1429–1438.

Blab GA, Cognet L, Berciaud S, et al. (2006). Optical readout of gold nanoparticle-based DNA microarrays without silver enhancement. Biophys J 90:L13–L15.

Bogart LK, Taylor A, Cesbron Y, et al. (2012). Photothermal microscopy of the core of dextran-coated iron oxide nanoparticles during cell uptake. ACS Nano 6:5961–5971.

Brusnichkin AV, Nedosekin DA, Galanzha EI, et al. (2010). Ultrasensitive label-free photothermal imaging, spectral identification, and quantification of cytochrome c in mitochondria, live cells, and solutions. J Biophoton 3:791–806.

Cognet L, Berciaud S, Lasne D, Lounis B. (2008). Photothermal methods for single nonluminescent nano-objects. Analyt Chem 80: 2288–2294.

Cognet L, Tardin C, Boyer D, et al. (2003). Single metallic nanoparticle imaging for protein detection in cells. Proc Natl Acad Sci USA 100: 11350–11355.

Coll J-L. (2010). Cancer optical imaging using fluorescent nanoparticles. Nanomedicine 6:7–10.

Gaiduk A, Yorulmaz M, Ruijgrok PV, Orrit M. (2010). Room-temperature detection of a single molecule's absorption by photothermal contrast. Science 330:353–356.

Galanzha E, Zharov V. (2013). Circulating tumor cell detection and capture by photoacoustic flow cytometry in vivo and ex vivo. Cancers 5:1691–1738.

Galanzha EI, Zharov VP. (2012). Photoacoustic flow cytometry. Methods 57:280–296.

Jayanna PK, Bedi D, Gillespie JW, et al. (2010). Landscape phage fusion protein-mediated targeting of nanomedicines enhances their prostate tumor cell association and cytotoxic efficiency. Nanomedicine Nanotechnol Biol Med 6:538–546.

Kimura H, Sekiguchi K, Kitamori T, et al. (2001). Assay of spherical cell surface molecules by thermal lens microscopy and its application to blood cell substances. Analyt Chem 73: 4333–4337.

Lasne D, Blab GA, Berciaud S, et al. (2006). Single nanoparticle photothermal tracking (SNaPT) of 5-nm gold beads in live cells. Biophys J 91:4598–4604.

Leduc C, Jung J-M, Carney RR, et al. (2011). Direct investigation of intracellular presence of gold nanoparticles via photothermal heterodyne imaging. ACS Nano 5:2587–2592.

Lee JS, Tung C-H. (2012). Enhancing the cellular delivery of nanoparticles using lipo-oligoarginine peptides. Adv Funct Mater 22:4924–4930.

Mérian J, Gravier J, Navarro F, Texier I. (2012). Fluorescent nanoprobes dedicated to in vivo imaging: From preclinical validations to clinical translation. Molecules 17:5564–5591.

Moreau J, Loriette V. (2006). Confocal dual-beam thermal-lens microscope: Model and experimental results. Jpn J Appl Phys Part 1 45: 7141–7151.

Mustafa T, Zhang Y, Watanabe F, et al. (2013). Iron oxide nanoparticle-based radio-frequency thermotherapy for human breast adenocarcinoma cancer cells. Biomater Sci 1: 870–880.

Nedosekin DA, Galanzha EI, Ayyadevara S, et al. (2012). Photothermal confocal spectromicroscopy of multiple cellular chromophores and fluorophores. Biophys J 102:672–681.

Nedosekin DA, Galanzha EI, Dervishi E, et al. (2014). Super-resolution nonlinear photothermal microscopy. Small 10:135–142.

Nedosekin DA, Juratli MA, Sarimollaoglu M, et al. (2013a). Photoacoustic and photothermal detection of circulating tumor cells, bacteria and nanoparticles in cerebrospinal fluid in vivo and ex vivo. J Biophoton 6:523–533.

Nedosekin DA, Sarimollaoglu M, Galanzha EI, et al. (2013b). Synergy of photoacoustic and fluorescence flow cytometry of circulating cells with negative and positive contrasts. J Biophoton 6: 425–434.

Nedosekin DA, Shashkov EV, Galanzha EI, et al. (2010). Photothermal multispectral image cytometry for quantitative histology of nanoparticles and micrometastasis in intact, stained and selectively burned tissues. Cytometry Part A 77A: 1049–1058.

Nima ZA, Mahmood M, Xu Y, et al. (2014). Circulating tumor cell identification by functionalized silver-gold nanorods with multicolor, super-enhanced SERS and photothermal resonances. Sci Rep 4: 4752.

Nima ZA, Mahmood MW, Karmakar A, et al. (2013). Single-walled carbon nanotubes as specific targeting and Raman spectroscopic agents for detection and discrimination of single human breast cancer cells. J Biomed Opt 18:55003.

Ntziachristos V. (2010). Going deeper than microscopy: The optical imaging frontier in biology. Nat Methods 7:603–614.

Saeed LM, Mahmood M, Pyrek SJ, et al. (2014). Single-walled carbon nanotube and graphene nanodelivery of gambogic acid increases its cytotoxicity in breast and pancreatic cancer cells. J Appl Toxicol 34: 1188–1199.

Sathuluri RR, Yoshikawa H, Shimizu E, et al. (2011). Gold nanoparticle-based surface-enhanced raman scattering for noninvasive molecular probing of embryonic stem cell differentiation. PLoS One 6: e22802.

Selmke M, Braun M, Cichos F. (2012a). Nano-lens diffraction around a single heated nano particle. Opt Express 20: 8055–8070.

Selmke M, Braun M, Cichos F. (2012b). Photothermal single-particle microscopy: Detection of a nanolens. Acs Nano 6: 2741–2749.

Shao J, Griffin RJ, Galanzha EI, et al. (2013). Photothermal nanodrugs: Potential of TNF-gold nanospheres for cancer theranostics. Sci Rep 3: 1293.

Thoumine O, Ewers H, Heine M, et al. (2008). Probing the dynamics of protein-protein interactions at neuronal contacts by optical imaging. Chem Rev 108:1565–1587.

Van Dijk MA, Tchebotareva AL, Orrit M, et al. (2006). Absorption and scattering microscopy of single metal nanoparticles. Phys Chem Chem Phys 8:3486–3495.

Wang LV, Hu S. (2012). Photoacoustic tomography: In vivo imaging from organelles to organs. Science 335:1458–1462.

Weinkauf H, Brehm-Stecher BF. (2009). Enhanced dark field microscopy for rapid artifact-free detection of nanoparticle binding to *Candida albicans* cells and hyphae. Biotechnol J 4: 871–879.

Zhang YB, Petibone D, Xu Y, et al. (2014). Toxicity and efficacy of carbon nanotubes and graphene: The utility of carbon-based nanoparticles in nanomedicine. Drug Metab Rev 46: 232–246.

Zharov VP. (2011). Ultrasharp nonlinear photothermal and photoacoustic resonances and holes beyond the spectral limit. Nat Photon 5: 110–116.

Zharov VP, Galitovskiy V, Lyle CS, Chambers TC. (2006a). Superhigh-sensitivity photothermal monitoring of individual cell response to antitumor drug. J Biomed Opt 11:064034.

Zharov VP, Galitovsky V, Chowdhury P. (2005). Nanocluster model of photothermal assay: Application for high-sensitive monitoring of nicotine-induced changes in metabolism, apoptosis, and necrosis at a cellular level. J Biomed Opt 10:44011.

Zharov VP, Galitovsky V, Viegas M. (2003). Photothermal detection of local thermal effects during selective nanophotothermolysis. Appl Phys Lett 83:4897–4899.

Zharov VP, Lapotko DO. (2005). Photothermal imaging of nanoparticles and cells. IEEE J Select Top Quantum Electron 11:733–751.

Zharov VP, Mercer KE, Galitovskaya EN, Smeltzer MS. (2006b). Photothermal nanotherapeutics and nanodiagnostics for selective killing of bacteria targeted with gold nanoparticles. Biophys J 90: 619–627.

Supplementary material available online

Supplemental Videos S1–S3.